Prediction of the two-dimensional Janus ferrovalley material LaBrI

Peng Jiang [1,2,3] Lili Kang [2] Yan-Ling Li [1] Xiaohong Zheng,[2,*] Zhi Zeng,[2] and Stefano Sanvito[3,†]

[1]*School of Physics and Electronic Engineering, Jiangsu Normal University, Xuzhou 221116, China*
[2]*Key Laboratory of Materials Physics, Institute of Solid State Physics, HFIPS, Chinese Academy of Sciences, Hefei 230031, China*
[3]*School of Physics and CRANN Institute, Trinity College, Dublin 2, Dublin, Ireland*

Two-dimensional (2D) ferrovalley materials, displaying coexistence of spontaneous spin and valley polarizations, have recently attracted significant attention due to their potential for applications in the fields of spintronics and valleytronics. However, unfortunately, to date only a few 2D ferrovalley materials exist. Here, first-principles calculations predict a 2D Janus ferrovalley material lanthanum bromiodide (LaBrI). It is found that LaBrI is a stable ferromagnetic electride, whose magnetic moment originates mainly from the interstitial anionic electrons. The magnetic transition temperature of LaBrI monolayers is estimated to be far beyond room temperature, and a sizable magnetic anisotropy with easy in-plane magnetization is also present. Most importantly, LaBrI monolayers exhibit a large valley polarization due to the concurrent broken space- and time-reversal symmetries, with the calculated valley polarization reaching up to 59 meV. This value is comparable to that of the ferrovalley materials reported to date. Intriguingly, the inequivalent Berry curvature at the two valleys takes opposite values, giving rise to an anomalous valley Hall effect, where a valley current with an accompanying net charge Hall current may be induced.

I. INTRODUCTION

The recent isolation of various 2D monolayers with hexagonal lattice structure, such as graphene, silicene, and group-VI transition-metal dichalcogenides (TMDCs), has open the possibility of a practical implementation of valleytronics. This aims at encoding, transferring, and storing information by using the valley degree of freedom. Valleytronics is, thus, underpinned by the fact that intervalley scattering between two well-separated valleys, labeled as K and $-K$ in momentum space, is negligible [1–6]. As a consequence, the valley index is a good quantum number and it can be considered as a binary pseudospin with a behavior similar to that of the actual spin degree of freedom. In this context, some interesting effects such as valley polarization and anomalous valley Hall effect (AVHE), based on the valley degree of freedom, have been intensively investigated in 2D hexagonal materials [7–9]. The practical realization of the above phenomena hinges on whether or not one is able to achieve valley-specific properties that differ at the K and $-K$ valley, in particular on lifting the degeneracy in energy or in the Berry curvature [10].

To this end, a number of attempts at lifting the valley degeneracy have been made in 2D hexagonal systems by using various external stimuli, such as an external magnetic field [11], optical pumping [7,12,13], magnetic doping [14–16], and magnetic proximity effect [17–20]. Although these strategies can indeed all induce valley polarization, they also have apparent disadvantages. An external magnetic field can break the valley degeneracy via valley-Zeeman splitting.

However, a sizable valley splitting requires extremely large field strengths, unrealistic in practical applications [21]. Optical pumping is a dynamical process and, as such, is not available for storing information. Magnetic doping is likely to result in impurity clustering and certainly increases the electron scattering rate. Magnetic proximity requires a magnetic substrate, so that the complexity of potential devices is significantly enhanced. Such disadvantages, present in all these proposals, naturally call for the search of 2D materials with an intrinsic valley polarization.

Very recently, a ferrovalley material concept was proposed for the $2H$-VSe$_2$ monolayer [22]. In this case the ferrovalley material not only shows spontaneous valley polarization but also exhibits intrinsic ferromagnetism. Most intriguingly, in $2H$-VSe$_2$ the valley polarization is coupled to the magnetic order, so that the valley polarity can be reversed by reversing the intrinsic magnetization. Thus, when compared to traditional 2D valleytronic materials, the ferrovalley ones have the potential to eliminate the limitations associated with external fields in inducing the valley polarization. This makes them an emerging materials subclass for next-generation nonvolatile memories. To date, ferrovalley materials with coexistence of spin and valley polarizations are only found in very few 2D hexagonal systems, such as $2H$-VSe$_2$ [22], $2H$-LaBr$_2$ [23], Nb$_3$I$_8$ [24], and Jauns $2H$-VSSe [25]. Thus, the search for more 2D ferrovalley materials with a large valley polarization and a high magnetic transition temperature is an important goal in condensed matter physics.

Recent experiments have demonstrated that Janus TMDCs can be successfully synthesized by controlling the reaction conditions [26,27]. Besides, some 2D magnetic Janus materials, such as chromium trihalides [28], manganese dichalcogenides [29], Cr$_2$O$_2$XY ($X = $ Cl, $Y = $ Br/I) [30],

CrO*X* (*X* = Cl, Br), etc. [31], have been proposed based on first-principles calculations. The intrinsic magnetism and broken inversion symmetry in these materials inspired us to speculate that large valley polarization can exist in the 2D magnetic Janus materials. Motivated by the recent experimental progresses in the synthesis of monolayer Janus materials and of bulk 2*H*-LaBr$_2$, and by the theoretical study of 2*H*-LaBr$_2$ monolayers [26,27,32,33], we propose and investigate a new 2D Janus monolayer ferrovalley material LaBrI. State-of-the-art first-principles total-energy calculations, combined with *ab initio* molecular dynamics, demonstrate that LaBrI monolayer is a thermodynamically stable ferromagnetic electride with a high transition temperature above room temperature and a sizable magnetic anisotropy energy (MAE). Remarkably, LaBrI shows a large valley polarization of about 59 meV, which is attributed to broken time-reversal and space-inversion symmetries. Notably, an external in-plane electric field can induce a spin-polarized anomalous valley-Hall effect.

II. COMPUTATIONAL METHODS AND DETAILS

Electronic structure calculations are performed by using the Vienna *ab initio* simulation package (VASP) [34,35], which is based on density functional theory (DFT) implemented over a plane-wave basis set with the projector-augmented wave method [36]. The plane-wave energy cutoff is set to 500 eV. As a matter of convention the 2D material lies in the *a-b* plane and along the out-of-plane direction (*c/z* axis) a vacuum region of no less than 15 Å is always included in the simulation cell. Dipole corrections are adopted to eliminate the effect of the spurious electric field due to the intrinsic electrical polarization. For structural optimization, the generalized gradient approximation (GGA) of Perdew-Burke-Ernzerhof (PBE) [37] is employed. The Brillouin zone (BZ) is sampled using a Γ-centered Monkhorst-Pack scheme with $12 \times 12 \times 1$ *k*-points grid and the convergence tolerance for the forces on each atom is 1 meV/Å. At the optimized structure the HSE06 hybrid functional [38] is used to calculate the electronic and magnetic properties of the predicted system. To check the dynamical stability of the ferromagnetic ground state of the LaBrI monolayer, a $4 \times 4 \times 1$ supercell is adopted to calculate the phonon spectrum by using the Phonopy code implementing the finite displacement method [39]. *Ab initio* molecular dynamics (AIMD) simulations in the canonical *NVT* ensemble are then performed to verify the thermodynamic stability. These last for 10 ps (time step = 2 fs) at $T = 500$ K. The Berry curvature is calculated by using the maximally localized Wannier function method as implemented in the WANNIER90 (v2.1) code [40], where the *p* orbitals of I and Br and the *d* orbitals of La are chosen as projected orbitals. In order to perform the Wannierization procedure, a frozen energy window of $[-8.5, 0.0]$ eV and an outer window of $[-10.0, 2.0]$ eV are chosen so to contain the low energy region. The minimum and maximal spread of the atomic orbitals are 1.93 and 6.49 Å^2, respectively. The relatively larger spread of the Wannier orbitals is due to the nature of the anionic electron with localized body, which is similar to what observed in LaBr$_2$ monolayer [41].

III. RESULTS AND DISCUSSION

Figures 1(a) and 1(b) display the fully relaxed structure of 2D Janus LaBrI monolayer. Similarly to 2*H*-MoSSe [26,27], Janus LaBrI monolayer in the 2*H* phase belongs to the *P*3*m*1 (No. 156) space group. The lattice constant, calculated at the PBE level, is 4.24 Å, while the layer thickness *d* is 4.02 Å and the corresponding bond lengths are 3.08 and 3.26 Å for the La-Br and La-I bond, respectively. The bond angles θ_1 and θ_2, shown in Fig. 1(b), are 87.0° and 81.2°, respectively. Considering the formal valence states of La^{3+}, Br^{-}, and I^{-}, there is one extra electron trapped in the lattice interstitial spaces, similarly to the case of 2*H*-LaBr$_2$ [33]. This unique feature is demonstrated by calculating the electron localization function (ELF), shown in Figs. 1(d) and 1(e). The ELF can often be used to determine the bonding character and the degree of the electron localization, with its value being between 0 and 1. Here ELF = 0 corresponds to no electron distribution and ELF = 0.5 to a homogeneous electron gas. In contrast, ELF = 1 is for a fully localized electron at a specific site. From Figs. 1(d) and 1(e) we find that the electrons are located over I/Br atoms, but also in the interstitial region between La ions. This indicates the LaBrI monolayer is a typical electride, where the intrinsic excess of charge is loosely localized in the lattice cavities.

The thermodynamical stability of the Janus LaBrI monolayer is assessed first by calculating its formation energy, which is defined as $E_{for} = (E_{LaBrI} - \mu_{La} - \mu_{Br} - \mu_{I})/3$. Here E_{LaBrI} is the total energy of the LaBrI ground state, and μ_{La}, μ_{Br}, and μ_{I} are the energy per atom of La, Br, and I in their most stable phases, respectively. It is found that E_{for} is about -1.92 eV/atom, meaning that the LaBrI monolayer has a good thermodynamical stability against the elemental phases. Then, to determine the ground geometry, here we consider other four different phases, namely 1*T* phase, *Pmmn*-phase 1, *Pmmn*-phase 2, and one mixed phase. The corresponding atomic structures are shown in Fig. S1 of the Supplemental Material (SM) [42]. The total energies of all these phases have been computed at the HSE06 level and shown in Table S1 in the SM [42]. It is found that the 2*H* phase is the lowest in energy, 0.18 eV/f.u. lower than the mix phase, 0.3 eV/f.u. lower than the 1*T* phase, 0.75 eV/f.u. lower than the *Pmmn*-phase 1, and 0.83 eV/f.u. lower than the *Pmmn*-phase 2. This result demonstrates that 2*H* phase is the most stable one, among the most probable.

In order to determine the structural stability of LaBrI in the monolayer form, the phonon dispersion spectrum is first computed and presented in Fig. 1(f). It is clearly seen that no imaginary frequencies are present across the BZ, demonstrating that 2D Janus LaBrI is dynamically stable. An AIMD simulation is further performed for 10 ps at $T = 500$ K and the results are shown in Fig. 1(g). It is found that the total energy fluctuates only slightly during the entire simulation, but the structure never develops any instability leading to reconstruction, as confirmed by a snapshot of the atomic structure at 10 ps [inset of Fig. 1(g)]. These results indicate that LaBrI has good thermal stability and it is structurally robust. Then, its mechanical properties are also investigated. For 2D hexagonal systems, there are two independent elastic constants, namely C_{11} and C_{12}, while C_{11} is equal to C_{22}, and
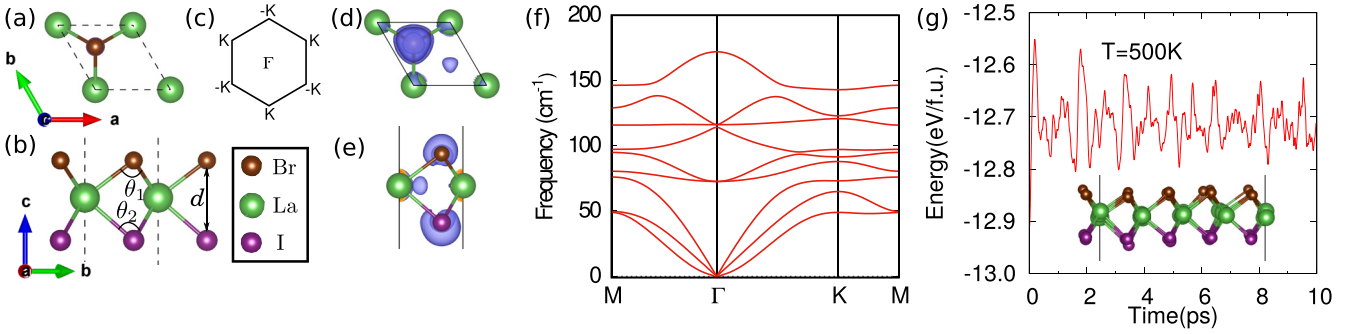
FIG. 1. (a) Top and (b) side views of the 2D Janus LaBrI monolayer. (c) The Brillouin zone of a generic 2D hexagonal system. (d) Top and (e) side views of the 3D spatial ELF of the LaBrI monolayer with the isovalue taken to 0.7. (f) The phonon dispersion of the LaBrI monolayer. (g) Variation of the total energy (eV/f.u.) with the simulation time in a AIMD run at 500 K. The inset shows a snapshot of the structure after 10 ps.

$C_{66} = (C_{11} - C_{12})/2$. According to the standard Voigt notation [43], we calculate the elastic constants of the LaBrI monolayer based on the energy-strain method [44]. The calculated C_{11}, C_{12}, C_{66} are found to be 30.38, 9.06, 10.66 N/m, respectively. These values meet the criteria of mechanical stability for a 2D hexagonal system [45,46], namely $C_{11} > 0$ and $C_{11} > |C_{12}|$. This further demonstrates that 2D Janus LaBrI monolayer is mechanically stable.

Next, we investigate the magnetic properties, which are computed at the level of HSE06 hybrid functional. The most stable magnetic configuration is determined by comparing the total energy of three different collinear magnetic structures, possible in a $2 \times 2 \times 1$ supercell, namely ferromagnetic (FM), antiferromagnetic (AFM), and nonmagnetic (NM). Our results show that the total energy of the FM state is the lowest, with an energy gain of 28.4 meV/f.u. over the AFM state and of 305.2 meV/f.u. over the NM one. In addition, we also consider a noncollinear 120° AFM configuration (see Fig. S2 in the SM [42]), obtained by constraining the initial direction of the magnetic moments. We find that such spin configuration is unstable and finally converges to the FM order, similarly to what observed for 2H-VSSe monolayers [25]. These findings provide a strong indication that the ground state is actually ferromagnetic, which is different from the noncollinear 120° AFM order found in other 2D triangular systems, such as 1T-VSTe [47], Cr/MoS₂, Fe/MoS₂, and Fe/WSe₂ interfaces [48]. A visual representation of the spatial distribution of the spin-polarized electrons can be obtained by plotting in 3D the real-space spin density, as done in Fig. 2(a). The figure clearly shows that the magnetic moment is localized in the interstitial region between the La atoms. The magnetic moment at the La site is 0.36 μ_B, while it is negligible at the I and Br sites. This feature is in line with the unique behavior of electride electrons, but totally different from that of most magnetic materials, where the spin density mainly localizes on the magnetic ions due to the partially filled 3d orbitals (or 4f) [22,25,49].

Thus the origin of the magnetic moment of the 2D Janus LaBrI monolayer is completely different from that of standard 3d-based ferromagnets. Nevertheless, the mechanism sustaining the magnetism can be reconducted to the conventional Stoner criterion [50], namely itinerant magnetism can be obtained if the inequality $ID(E_F) > 1$ is satisfied,

where I is the Stoner exchange interaction parameter and $D(E_F)$ is the density of states (DOS) at the Fermi level E_F for the associated diamagnetic system. Here the Stoner exchange parameter can be obtained from the band spin split Δ_{ex} as $\Delta_{ex} = I m_{avg}$, where m_{avg} is the magnetic moment per magnetic atom [51]. In order to determine whether or not LaBrI meets the Stoner criterion, we first present the nonspin-polarized band structure [see Fig. 2(b)] and the associated partial charge density and projected DOS (PDOS). It is found that a half-filled energy band crosses the Fermi level, resulting in metallicity. Such half-filled band originates mainly from the excess electrons localized in the interstitial regions, with little contribution from the La-d orbitals, as it can be revealed by the PDOS of Fig. 2(c). This result indicates that LaBrI is a zero-dimensional (0D) electride with the anionic electron excess confined in the 0D cavity. The LaBrI unit cell can thus be written as the chemical formula of an electride, namely $[LaBrI]^+ \cdot e^-$. It has been previously demonstrated that, due to quantum confinement effects, the itinerant anionic electrons trapped in the cavities could result in a large DOS near E_F [see Fig. 2(c)], leading to a Stoner-type magnetic instability [33,49]. We then compute I and $D(E_F)$ and obtain values of 1.61 and 4.43, respectively, which clearly confirms that $ID(E_F) > 1$. Magnetism is then is attributed to the instability of the confined interstitial electrons in the LaBrI monolayer.

After having understood the origin of the spontaneous ferromagnetism, we investigate the electronic properties of such FM state. Figure 2(c) shows the spin-polarized band structure of the FM LaBrI monolayer, computed without considering spin-orbit coupling (SOC). The spin polarization splits the metallic band at E_F, making the materials a ferromagnetic insulator with an indirect band gap of 1.05 eV and a moment per unit cell of 1.0 μ_B. This electronic structure agrees well with the one-electron charge excess of $[LaBrI]^+ \cdot e^-$. Since the gap is between the two spin components of the original singlet band, the orbital contributions of the valence band maximum (VBM) and the conduction band minimum (CBM) near Fermi level for FM state are the the same as those of the singlet band crossing Fermi level for NM state [see Fig. 2(d)]. Moreover, the VBM and the CBM possess opposite spin polarization, so that LaBrI is a spin semiconductor, also known as a bipolar magnetic semiconductor [52–54]. For electronic structures of this type, electric control of the spin polarization at the Fermi
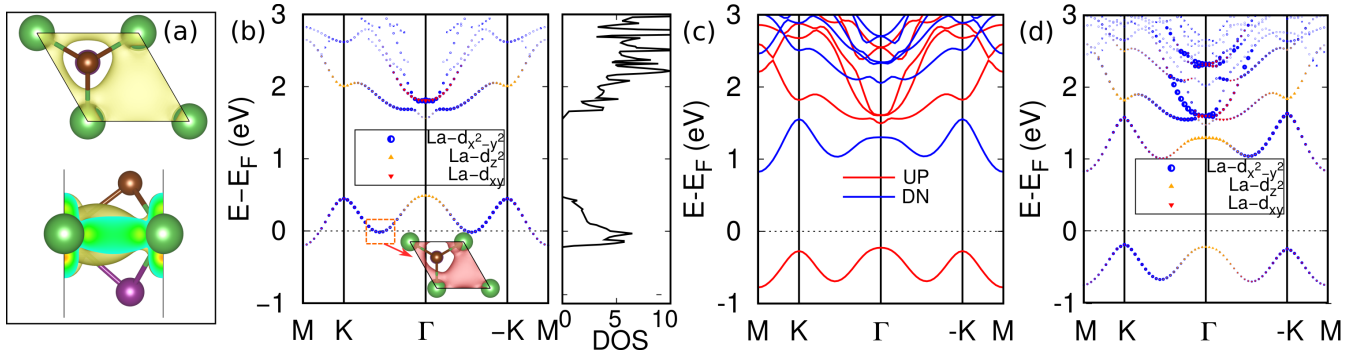
FIG. 2. (a) Top and side views of 3D spin density of the LaBrI monolayer with the isosurface value set as 0.008 e/bohr^3. (b) The orbital-projected band structure and DOS of the LaBrI monolayer in the NM state. The inset shows the partial charge density of the metallic band near the Fermi level with the isosurface value set as 0.008 e/bohr^3. The (c) nonprojected and (d) projected spin-polarized band structure of the LaBrI monolayer in the FM ground state.

level, namely the transition between an insulating and a half-metal state, can be achieved by applying an appropriate gate voltage [52].

Although some intrinsic 2D FM semiconductors, such as CrI$_3$ [55] and Cr$_2$Ge$_2$Te$_6$ [56], have been discovered experimentally, their relatively low Curie temperatures severely hinder a possible use in practical applications. Hence, 2D intrinsic ferromagnets with a high Curie temperature are still very important and in high demand. For this reason we perform a full characterization of the magnetic properties of LaBrI monolayers, by computing first the MAE and then the critical temperature. The MAE is defined as the difference in total energy between the configurations where the magnetization axis is along the in-plane (100) or along the out-of-plane (001) direction, namely $E_{MAE} = E_{100} - E_{001}$. Since the magnetocrystalline anisotropy microscopically originates from the SOC interaction, SOC is considered when computing the MAE. When using the HSE06 functional we find $E_{MAE} = -100$ μeV/La, which is significantly higher than what is typically found for many elemental ferromagnetic metals (Fe, Co, and Ni) [57]. A negative MAE sign means that the magnetization is preferentially in the layer plane (*a-b* plane). Furthermore, we were not able to resolve any further anisotropy by rotating the magnetization in-plane, so that the system possesses a hard-axis easy-plane magnetic configuration, and can be described as a 2D *XY* magnet.

The Curie temperature or a more generic magnetic transition temperature is another important criterion for evaluating the magnetic stability of 2D FM crystals. For a 2D *XY* magnet, a Berezinskii-Kosterlitz-Thouless (BKT) magnetic transition can be observed at a critical temperature T_C. Recent Monte Carlo simulations [58] have demonstrated that the T_C of a 2D *XY* triangular system can be estimated to be 1.335 J/k_B, which is about 1.5 times larger than that of 2D square lattice ($T_C = 0.89$ J/k_B) [59]. Here J and k_B are the nearest-neighbor (NN) exchange parameter and the Boltzmann constant, respectively. In our case J can be obtained from the energy difference between the FM and the AFM states, namely as $J = (E_{AFM} - E_{FM})/8S^2$, where $S = M_{total}/2 = \frac{1}{2}$. Then our estimated T_C, as obtained with HSE06, is about 880 K, significantly higher than that of most reported 2D intrinsic ferromagnets [55,56]. Furthermore, our AIMD simulations, shown in Fig. S3 of the SM, demonstrate that the

ferromagnetic order is maintained against atomic vibrations at 500 K [42]. Therefore, in concluding this section, we remark that the sizable MAE and the high T_C make the 2D Janus LaBrI monolayer a promising candidate for applications in room-temperature spintronic devices.

A final striking feature of LaBrI is the presence of valley polarization at the K and $-K$ points, with our HSE06-calculated results shown in Fig. 3. When SOC is switched off [see Figs. 2(a) and 2(b)], we find that the two inequivalent K and $-K$ points are energetically degenerate in both the nonspin-polarized and spin-polarized cases. The inclusion of SOC lifts the energy degeneracy between the K and $-K$ points and their energy splits depend on the direction of the magnetization. In fact, we find that the band maximum at K is 59 meV higher than that at $-K$ when the magnetization points along the z direction, while the situation is reversed when the magnetization is rotated along the $-z$ direction. Such band split of 59 meV is larger than that found for the LaBr$_2$ monolayer [23], indicating that the Janus structure plays a role.

The comparison between the DFT band structure and the Wannier one is shown in Fig. S4 of the SM [42]. It is clear that the calculated HSE06 bands are well consistent with those obtained by Wannier fitting. Then we compute the Berry curvature $\Omega(k)$, of LaBrI, a quantity that is usually utilized to determine the electronic transport properties of materials.
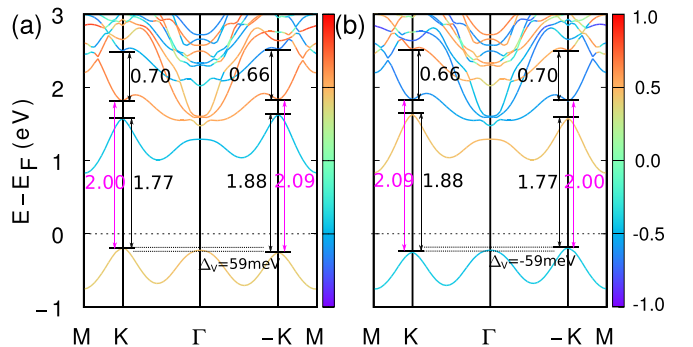

FIG. 3. The band structures of 2D Janus LaBrI monolayer computed by including SOC: the magnetization direction is along (a) +z axis and (b) −z axis. The out-of-plane spin component S_z is denoted by color.
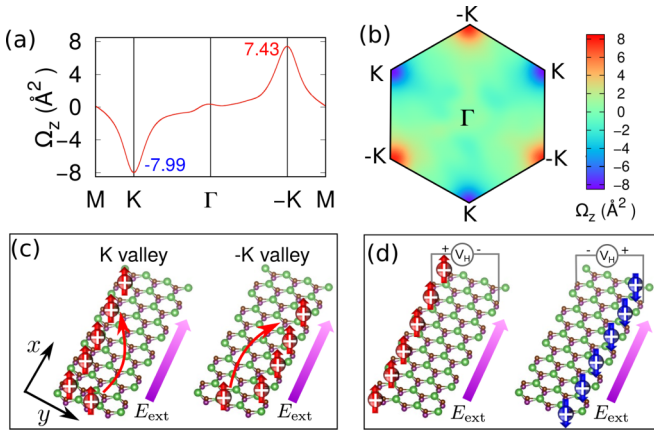
FIG. 4. The Berry curvature Ω_z of the LaBrI monolayer computed: (a) along the high symmetry lines, and (b) over the 2D Brillouin zone. (c) Schematic diagrams of the AVHE for the K and $-K$ carriers in the hole-doped LaBrI monolayer when the direction of the magnetic moment is along $+z$ axis. (d) Schematic diagrams of the Hall voltages for hole-doped LaBrI monolayer when the magnetic moment is along $+z$ (left plot) and $-z$ (right plot) direction, respectively. The red and blue spheres in (c) and (d) denote the spin-up and spin-down components, respectively.

Here $\Omega(k)$ is calculated from the Kubo formula [60] as

$$\Omega(k) = -\sum_n f_n \sum_{n' \neq n} \frac{2\,\mathrm{Im}\langle \psi_{nk}|\hat{v}_x|\psi_{n'k}\rangle\langle \psi_{n'k}|\hat{v}_y|\psi_{nk}\rangle}{(E_{n'} - E_n)^2}, \quad (1)$$

where the sum is over all the valence bands n, f_n is the Fermi-Dirac distribution function, $|\psi_{nk}\rangle$ is the wave function associated with the eigenvalue E_n, and $\hat{v}_x$ and $\hat{v}_y$ are the velocity operators along the x and y direction, respectively. Figures 4(a) and 4(b) show the calculated Berry curvatures Ω_z along the high-symmetry point and over the 2D Brillouin zone, respectively, when the magnetic moment is along $+z$ direction.

We find that a nonzero Berry curvature is observed mainly around the K and $-K$ points, where $\Omega(k)$ takes opposite signs although not identical absolute values [$\Omega(K)$: -7.99 Å^2 and $\Omega(-K)$: 7.43 Å^2]. This is well consistent with the unique electronic structure of ferrovalley materials [22]. As a consequence, when holes are injected in the monolayer and a longitudinal electric field is applied, the carriers at the K and

$-K$ valleys develop opposite transverse anomalous velocities, since $v_a \propto E \times \Omega$ [61]. This results in a spin-polarized AVHE, whose schematic diagram is given in Fig. 4(c). Moreover, since the absolute value of the Berry curvature at the K valley is larger than that at the $-K$ one, a net charge accumulation with a negative Hall voltage is expected, as shown in the left plot of Fig. 4(d). It is necessary to emphasize here that the reversal of the valley/spin polarization makes the absolute values of the Berry curvature at the K and $-K$ valleys to swap, but the sign of the Berry curvature remains unchanged. As such, reversing the magnetization will result in a sign change of the induced voltage, but will not alter its magnitude [see schematic diagram in the right plot of Fig. 4(d)].

IV. CONCLUSION

In summary, we have theoretically predicted a 2D monolayer with Janus structure LaBrI to be a 2D XY electride magnet, in which the excess anionic electrons are organized in a quasi-long-range FM phase. It is found that LaBrI exhibits indirect-gap semiconducting characteristics with a wide gap of 1.05 eV. In addition, the LaBrI monolayer displays easy in-plane magnetization with a sizable MAE, and a magnetic transition temperature up to 880 K. More interestingly, spontaneous valley polarization can be observed, with the intrinsic valley energy split reaching up 59 meV. Moreover, the Berry curvature at the two valleys has opposite sign and slightly different absolute value, resulting in the possibility of obtaining an anomalous valley Hall effect, where a valley current with an accompanying net charge Hall current is driven by a transverse electric field. All these features make the 2D Janus LaBrI monolayer a very promising material to develop intriguing spin-valley devices.

ACKNOWLEDGMENTS

[1] J. R. Schaibley, H. Yu, G. Clark, P. Rivera, J. S. Ross, K. L. Seyler, W. Yao, and X. Xu, Nat. Rev. Mater. **1**, 16055 (2016).

[2] X. Wu, Y. Meng, J. Tian, Y. Huang, H. Xiang, D. Han, and W. Wen, Nat. Commun. **8**, 1 (2017).

[3] X. Li, T. Cao, Q. Niu, J. Shi, and J. Feng, Proc. Natl Acad. Sci. U.S.A. **110**, 3738 (2013).

[4] T. Cao, G. Wang, W. Han, H. Ye, C. Zhu, J. Shi, Q. Niu, P. Tan, E. Wang, B. Liu et al., Nat. Commun. **3**, 887 (2012).

[5] G. Kioseoglou, A. Hanbicki, M. Currie, A. Friedman, D. Gunlycke, and B. Jonker, Appl. Phys. Lett. **101**, 221907 (2012).

[6] D. Xiao, W. Yao, and Q. Niu, Phys. Rev. Lett. **99**, 236809 (2007).

[7] H. Zeng, J. Dai, W. Yao, D. Xiao, and X. Cui, Nat. Nanotech. **7**, 490 (2012).

[8] H. Pan, Z. Li, C.-C. Liu, G. Zhu, Z. Qiao, and Y. Yao, Phys. Rev. Lett. **112**, 106802 (2014).

[9] J. Ding, Z. Qiao, W. Feng, Y. Yao, and Q. Niu, Phys. Rev. B **84**, 195444 (2011).

[10] S. Wu, J. S. Ross, G.-B. Liu, G. Aivazian, A. Jones, Z. Fei, W. Zhu, D. Xiao, W. Yao, D. Cobden et al., Nat. Phys. **9**, 149 (2013).

[11] T. Cai, S. A. Yang, X. Li, F. Zhang, J. Shi, W. Yao, and Q. Niu, Phys. Rev. B **88**, 115140 (2013).

[12] K. F. Mak, K. He, J. Shan, and T. F. Heinz, Nat. Nanotech. **7**, 494 (2012).

[13] Z. Ye, D. Sun, and T. F. Heinz, Nat. Phys. **13**, 26 (2017).

[14] Y. Cheng, Q. Zhang, and U. Schwingenschlögl, Phys. Rev. B **89**, 155429 (2014).

[15] N. Singh and U. Schwingenschlögl, Adv. Mater. **29**, 1600970 (2017).

[16] R. Peng, Y. Ma, S. Zhang, B. Huang, and Y. Dai, J. Phys. Chem. Lett. **9**, 3612 (2018).

[17] Q. Zhang, S. A. Yang, W. Mi, Y. Cheng, and U. Schwingenschlögl, Adv. Mater. **28**, 959 (2016).

[18] L. Xu, M. Yang, L. Shen, J. Zhou, T. Zhu, and Y. P. Feng, Phys. Rev. B **97**, 041405(R) (2018).

[19] T. Norden, C. Zhao, P. Zhang, R. Sabirianov, A. Petrou, and H. Zeng, Nat. Commun. **10**, 4163 (2019).

[20] T. Hu, G. Zhao, H. Gao, Y. Wu, J. Hong, A. Stroppa, and W. Ren, Phys. Rev. B **101**, 125401 (2020).

[21] A. Srivastava, M. Sidler, A. V. Allain, D. S. Lembke, A. Kis, and A. Imamoğlu, Nat. Phys. **11**, 141 (2015).

[22] W.-Y. Tong, S.-J. Gong, X. Wan, and C.-G. Duan, Nat. Commun. **7**, 1 (2016).

[23] P. Zhao, Y. Ma, C. Lei, H. Wang, B. Huang, and Y. Dai, Appl. Phys. Lett. **115**, 261605 (2019).

[24] R. Peng, Y. Ma, X. Xu, Z. He, B. Huang, and Y. Dai, Phys. Rev. B **102**, 035412 (2020).

[25] C. Zhang, Y. Nie, S. Sanvito, and A. Du, Nano Lett. **19**, 1366 (2019).

[26] A.-Y. Lu, H. Zhu, J. Xiao, C.-P. Chuu, Y. Han, M.-H. Chiu, C.-C. Cheng, C.-W. Yang, K.-H. Wei, Y. Yang *et al.*, Nat. Nanotech. **12**, 744 (2017).

[27] J. Zhang, S. Jia, I. Kholmanov, L. Dong, D. Er, W. Chen, H. Guo, Z. Jin, V. B. Shenoy, L. Shi *et al.*, ACS Nano **11**, 8192 (2017).

[28] C. Xu, J. Feng, S. Prokhorenko, Y. Nahas, H. Xiang, and L. Bellaiche, Phys. Rev. B **101**, 060404(R) (2020).

[29] J. Liang, W. Wang, H. Du, A. Hallal, K. Garcia, M. Chshiev, A. Fert, and H. Yang, Phys. Rev. B **101**, 184401 (2020).

[30] J. Jiao, N. Miao, Z. Li, Y. Gan, J. Zhou, and Z. Sun, J. Phys. Chem. Lett. **10**, 3922 (2019).

[31] N. Miao, B. Xu, L. Zhu, J. Zhou, and Z. Sun, J. Am. Chem. Soc. **140**, 2417 (2018).

[32] K. Krämer, T. Schleid, M. Schulze, W. Urland, and G. Meyer, Z. Anorg. Allg. Chem. **575**, 61 (1989).

[33] J. Zhou, L. Shen, M. Yang, H. Cheng, W. Kong, and Y. P. Feng, Chem. Mater. **31**, 1860 (2019).

[34] G. Kresse and J. Furthmüller, Phys. Rev. B **54**, 11169 (1996).

[35] G. Kresse and D. Joubert, Phys. Rev. B **59**, 1758 (1999).

[36] P. E. Blöchl, Phys. Rev. B **50**, 17953 (1994).

[37] J. P. Perdew, K. Burke, and M. Ernzerhof, Phy. Rev. Lett. **77**, 3865 (1996).

[38] J. Paier, M. Marsman, K. Hummer, G. Kresse, I. C. Gerber, and J. G. Ángyán, J. Chem. Phys. **124**, 154709 (2006).

[39] A. Togo and I. Tanaka, Scr. Mater. **108**, 1 (2015).

[40] A. A. Mostofi, J. R. Yates, G. Pizzi, Y.-S. Lee, I. Souza, D. Vanderbilt, and N. Marzari, Comput. Phys. Commun. **185**, 2309 (2014).

[41] J. Zhou, Y. P. Feng, and L. Shen, Phys. Rev. B **102**, 180407(R) (2020).

[42] See Supplemental Material at http://link.aps.org/supplemental/10.1103/PhysRevB.104.035430 for the possible structural phases; the different magnetic configurations; the calculated AIMD evolutions of the total magnetic moments; the comparison of the band structures obtained by DFT and the Wannier fitting.

[43] R. C. Andrew, R. E. Mapasha, A. M. Ukpong, and N. Chetty, Phys. Rev. B **85**, 125428 (2012).

[44] S. Zhang, J. Zhou, Q. Wang, X. Chen, Y. Kawazoe, and P. Jena, Proc. Natl. Acad. Sci. U.S.A. **112**, 2372 (2015).

[45] S. Haastrup, M. Strange, M. Pandey, T. Deilmann, P. S. Schmidt, N. F. Hinsche, M. N. Gjerding, D. Torelli, P. M. Larsen, A. C. Riis-Jensen *et al.*, 2D Mater. **5**, 042002 (2018).

[46] M. Maździarz, 2D Mater. **6**, 048001 (2019).

[47] D. Dey and A. S. Botana, Phys. Rev. Mater. **4**, 074002 (2020).

[48] W. Fang, A. Raeliarijaona, P.-H. Chang, A. A. Kovalev, and K. D. Belashchenko, Phys. Rev. Mater. **5**, 054401 (2021).

[49] X. Sui, J. Wang, and W. Duan, J. Phys. Chem. C **123**, 5003 (2019).

[50] E. C. Stoner, Proc. R. Soc. London Ser. A **169**, 339 (1939).

[51] P. Jiang, L. Kang, X. Zheng, Z. Zeng, and S. Sanvito, Phys. Rev. B **102**, 195408 (2020).

[52] X. Li and J. Yang, Phys. Chem. Chem. Phys. **15**, 15793 (2013).

[53] P. Jiang, X. Tao, H. Hao, L. Song, X. Zheng, and Z. Zeng, RSC Adv. **7**, 28124 (2017).

[54] P. Jiang, L. Kang, X. Tao, N. Cao, H. Hao, X. Zheng, L. Zhang, and Z. Zeng, J. Phys.: Condens. Matter **31**, 495701 (2019).

[55] B. Huang, G. Clark, E. Navarromoratalla, D. R. Klein, R. Cheng, K. L. Seyler, D. Zhong, E. Schmidgall, M. A. Mcguire, and D. H. Cobden, Nature (London) **546**, 270 (2017).

[56] C. Gong, L. Li, Z. Li, H. Ji, A. Stern, Y. Xia, T. Cao, W. Bao, C. Wang, Y. Wang, Z. Q. Qiu, R. J. Cava, S. G. Louie, J. Xia, and X. Zhang, Nature (London) **546**, 265 (2017).

[57] S. V. Halilov, A. Y. Perlov, P. M. Oppeneer, A. N. Yaresko, and V. N. Antonov, Phys. Rev. B **57**, 9557 (1998).

[58] S. Zhang, R. Xu, W. Duan, and X. Zou, Adv. Fun. Mater. **29**, 1808380 (2019).

[59] J. F. Fernández, M. F. Ferreira, and J. Stankiewicz, Phys. Rev. B **34**, 292 (1986).

[60] D. J. Thouless, M. Kohmoto, M. P. Nightingale, and M. den Nijs, Phys. Rev. Lett. **49**, 405 (1982).

[61] D. Xiao, M.-C. Chang, and Q. Niu, Rev. Mod. Phys. **82**, 1959 (2010).